# Highly sensitive SWIR detector array based on nanoscale phototransistors integrated on CMOS readout

**Lining Liu[1], Jacob Rabinowitz[1], Simone Bianconi[1], Min-Su Park[2], Hooman Mohseni[1]***

**AFFILIATIONS**

[1] Bio-Inspired Sensors and Optoelectronics Laboratory, Northwestern University, 2145 Sheridan Rd, Evanston, Illinois 60208, USA

[2] Department of Electronics Engineering, Dong-A University, Busan 49315, Republic of Korea

* Author to whom correspondence should be addressed: hmohseni@northwestern.edu

**ABSTRACT**

Ultra-sensitive and fast infrared imaging has become increasingly important in applications that require high frame rates at low light levels, such as exoplanet imaging. The sensitivity of conventional short-wave infrared cameras is limited by their read-out noise level. This limitation can be addressed by the internal gain of the sensors, but only if fast response time and low dark current are achieved simultaneously. Recent theoretical predictions suggested that reducing the internal capacitance of detectors with internal gain can increase their sensitivity. Here we show the experimental validation of this prediction for III-V heterojunction phototransistors. We have fabricated a 320 × 256 array of InGaAs/InP infrared phototransistors integrated with a conventional silicon readout circuit. The array is made of two groups of pixels; 50% are devices with 1 μm base diameters and the other 50% with 2 μm base diameter. Characterization of a large number of pixels show that 1 μm devices have significantly higher sensitivity than 2 μm devices. These have an average noise equivalent photon sensitivity of about 20 photons at a camera frame rate of ~500 FPS, which is better than the best existing infrared cameras with similar cutoff wavelength and frame rate. Interestingly, the processing variation in the 1 μm devices resulted in variation in sensitivity, and a good number of devices show sensitivity to less than 10 photons. These results suggest that the proposed phototransistors are promising for ultra-sensitive SWIR cameras.

Ultra-sensitive and fast detection for short-wavelength infrared (SWIR) is an essential requirement in an increasing number of applications, including quantum information processing, Raman spectroscopy, quantum cryptography, astronomical imaging, biological imaging, light detection and ranging (LiDAR), and optical time domain reflectometers (OTDRs)[1-5]. Single-photon imaging at thermoelectrically accessible temperatures (i.e. above ~200 K) is the ultimate goal. While tremendous efforts have been made to achieve single photon imaging using avalanche photodiodes (APD), photomultiplier tubes, quantum-dot field-effect transistors (QD-FET), resonant tunneling diodes (RTD)[2,6-10], there is still significant room for improvement. Beside the high sensitivity, there is great demand for high-speed infrared cameras, to achieve real-time imaging. For example, ground-based adaptive optics for astronomical imaging requires kHz speed to measure real-time atmospheric interference as well as high sensitivity to detect leftover starlight leaking around an occluding coronagraph[11]. Unfortunately, readout integrated circuits (ROIC) add significant noise to each frame, especially at high frame rates.

Currently, commercial SWIR imaging sensors are dominated by InGaAs PIN photodetectors, due to their low leakage current and short response time. They lack internal gain, however, so the high read-out noise (RON) from electronic circuitry limits further improvement in imaging sensitivity. So internal gain is necessary to amplify the signal above the RON floor. APDs can provide internal gain, but the avalanche multiplication process could produce a large excess noise factor. APDs also require a large operating voltage and show a large gain variation as a function of the bias voltage[12]. Low-dimensional photodetectors have achieved high internal gain, but their low speed is a fatal drawback[13-15] and their integration with large arrays of silicon electronics into a compact camera chip has been challenging. Heterojunction phototransistor (HPT) is one of the promising candidates to achieve a large enough internal gain. The small dark current combined with the CMOS-compatible low operational bias make HPT attractive for weak light detection when comparing with its PIN photodetector and APD counterparts. Electron-injection (EI) HPT detector has been studied and proved able to achieve a high avalanche-free amplification, and a high sensitivity thanks to its combination of a large-area absorbing layer and a nano-scale electron injector[16-19]. By leveraging the additional degrees of freedom in its geometry to decrease the

junction capacitance, the EI detector has achieved state-of-art SWIR detection performance for cameras and optical coherence tomography (OCT) systems[20,21].

This paper demonstrates a detector array based on InGaAs/InP HPT EI detectors bonded to a commercial ROIC. We developed a 320×256 detector array consisting of two devices with different base diameters: 2 μm (50%) and 1 μm (50%). The 1 μm detectors achieved an average sensitivity of less than 20 photons at 480 frames per second (FPS) on average, despite using a ROIC with a RON value of 500 electrons per frame. Interestingly, variations in the device fabrication led to variations of device sensitivity values and a good number of detectors exhibit much better sensitivity values (below 10 photons).

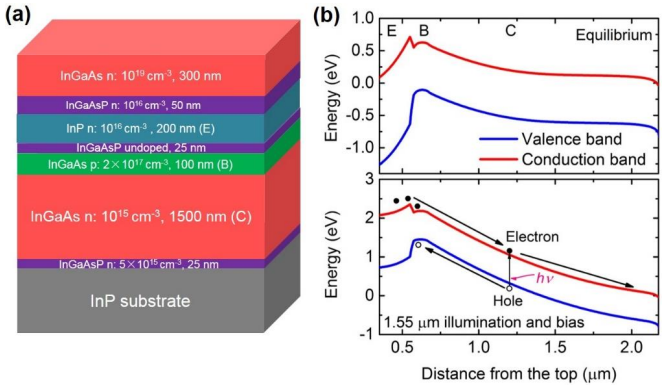


**Fig. 1** (a) Epitaxial layers for the HPT detectors in this work, (b) band structure of the epitaxial structure with and without bias.

The epitaxial layers (Fig. 1(a)) for the HPT detectors with an NPN structure were grown on sulfur-doped InP using Low-Pressure Metal-Organic Chemical Vapor Deposition (LP-MOCVD). The composition of InGaAs is $In_{0.47}Ga_{0.53}As$, while for InGaAsP, the x and y are graded in $In_xGa_{1-x}As_yP_{1-y}$ that vary from 0.47 to 1 and from 1 to 0, respectively from the InGaAs side to InP side. The undoped InGaAsP layer between the emitter and base acts as a transition layer for InP and InGaAs, which can decrease the barrier of electrons and thus increase the gain (See Supplementary I). Fig. 1(b) shows the band structure of the HPT detectors: under equilibrium, the p-type base layer can be an electron-blocking barrier, ensuring low dark current. Under illumination and

electric bias, the photo-generated holes transport to the base layer that traps holes and modulate its potential, lowering the barrier for electron injection from the emitter, enabling optical gain[22]. Fig. 2 demonstrates the fabrication process of the hybrid HPT detector array. The detector array was designed to have pixels with 1 μm injector in diameter in one region and 2 μm in the other for comparison. Non-alloyed Ti/Mo/Au (20/30/150 nm) emitter contact was evaporated and lifted-off to define these pillars. Combination of $CH_4/H_2$ based reactive-ion etching (RIE) dry etching and wet etching was used to etch till the top of the InGaAs collector. Then the optical window mesa ($26\times26$ $\mu m^2$ and pitch of 30 μm) was defined by wet etching in $H_3PO_4/H_2O_2/H_2O$. Subsequently, benzocyclobutene (BCB) spin coating and curing (250 °C) was implemented for passivation and planarization, followed by the etch-back of BCB. The InP substrate for ground contact was exposed by ground patterning etching. Ti/Ni/Au (20/30/100 nm) under bump metal (UBM) was then evaporated on the pillars and the ground area.

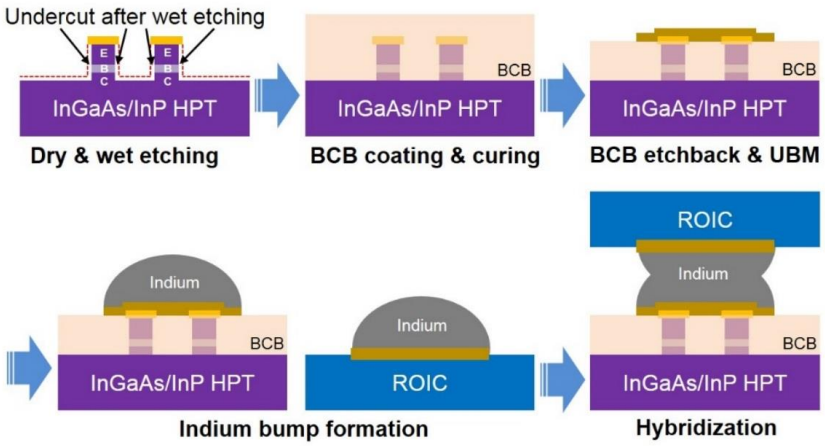


**Fig. 2** Schematic diagram of the fabrication process for the detector array.

The fabricated array was hybridized with a commercial ISC9809 ROIC (FLIR). To accomplish this, indium bumps were electroplated on the detector array and the ROIC from an Au seed layer. The photoresist and the Au seed layer were then removed by acetone and potassium cyanide solution respectively. The backside of the detector array sample was polished in order to improve

light coupling, followed by indium bump reflow in flux at 170 °C. Subsequently, the detector array and the ROIC were aligned and bonded at 100 °C, 20 kg using a flip-chip bonding machine. Finally, the hybridized sample was attached to a carrier chip where the ROIC metal pads were wire-bonded to.

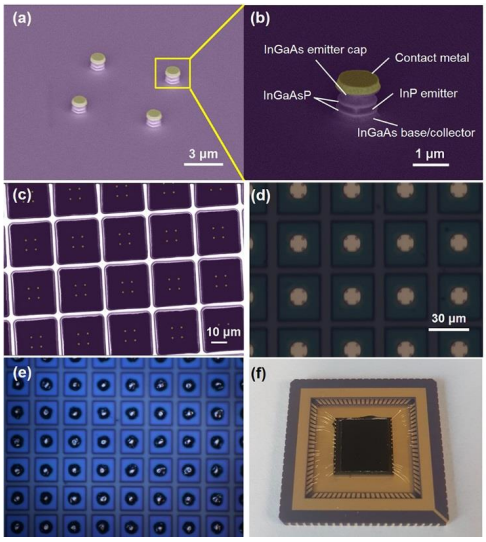


**Fig. 3** SEM images of (a) the 2×2 electron injectors in one pixel, (b) one electron injector showing the epitaxial layers, and (c) the detector array after the etch back of BCB. Microscope images of (d) the detector array after the deposition of UBM and (e) the indium bump formation, (f) detector array integrated with ROIC and wire bonded to the chip carrier for measurement.

SEM and microscope images of the detector array with 1 μm base diameter presented in this work are shown in Fig. 2. Each pixel contains 2×2 multi-electron injectors, designed to improve mechanical stability and fill-factor while maintaining a low capacitance. In Fig. 3(b), undercut can be observed in the injector[23,24]. This resulted from the wet etching process, which is used to remove the shallow crystalline damages of the sidewalls after the dry etching of the injector. Fig. 3(c) shows the SEM image after the etch-back of the BCB, in which the metal contact on top of the injectors are exposed. In Fig. 3(d) and Fig. 3(e), the 2×2 injectors in each pixel are connected by the UBM and indium bumps. For the purpose of measurement, the integrated detector array is wire bonded to the chip carrier (Fig. 3(f)), which is mounted to a liquid nitrogen vacuum dewar with an

internal heater for precise temperature control. The chip carrier is connected via feedthroughs to the camera head electronics, which powers and controls the ROIC and sends the recorded data to a computer for storage and further analysis. Wavelength of the light beam used for measurement is 1.55 µm.

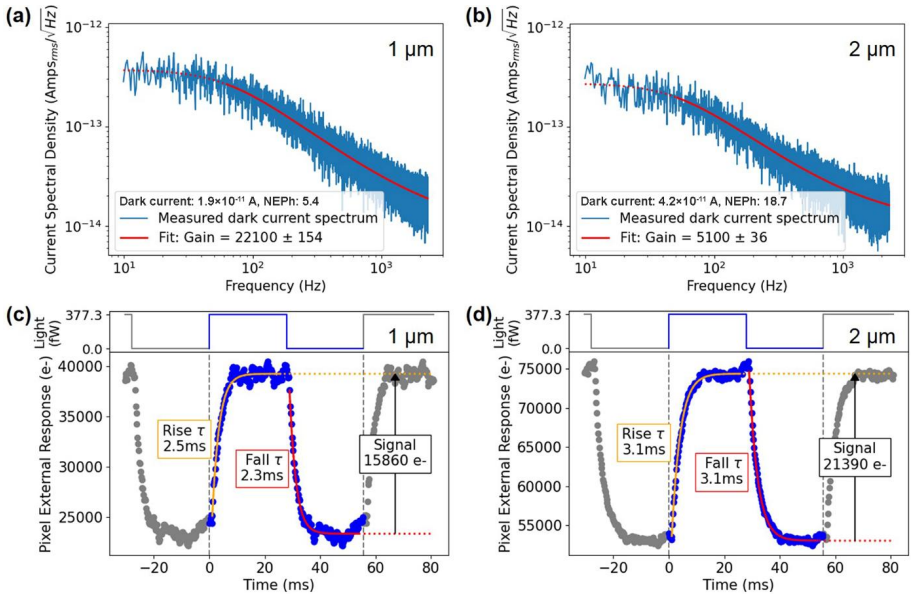


**Fig. 4** Example characteristics of 1 µm and 2 µm pixels at 200 K: Frequency spectrum of the dark current noise of (a) a 1 µm pixel (dark current: $1.9 \times 10^{-11}$ A) and (b) a 2 µm pixel (dark current: $4.2 \times 10^{-11}$ A). Response to a square-wave light pulse of 377 fW spread uniformly across the same (c) 1 µm pixel as (a) and (d) 2 µm pixel as (b). Frames were taken at 4590 Hz with a 202 µs integration time. Exponentials were fit to the rise and fall times to evaluate the response time of the detector.

To characterize the detectors, the internal gain ($G$) is investigated. Usually, this is extracted by first finding the external gain $G_{ex}$ (by illuminating the detector with a calibrated optical power and recording its response) and then using it to derive the internal gain. The two gains are related by $G = G_{ex}/(QE \times FF)$, where the quantum efficiency $QE$ presents the percentage of photons incident on a pixel area which are absorbed and generate free charge carriers, and the fill factor $FF$ represents the percentage of these photogenerated carriers which reach the pixel's electronically active area ("injector") – and are therefore detected – before recombining. However, in our case

the fill factor and quantum efficiency are not known, and in many cases the assumed value of the *QE* is not accurate[14,25,26]. Following well-established methods[27,28], we find the internal gain by directly measuring the device's noise. The frequency spectrum of the pixel's dark current is obtained by taking the Fourier transform of video frames saved at high frame rate (4590 FPS). Examples of spectra of a 1 μm and a 2 μm pixels are shown in Fig. 4(a) and Fig. 4(b). The time constant $\tau$ of the pixel results in a filtering effect that attenuates its white noise at high frequencies. As we discussed elsewhere[29], the noise current spectrum for a pixel with external dark current $I_{ex}$ is given by Eq. (1), in which both the dark current shot noise and the amplified dark current noise are both taken into account by including the gain.

$$i_{ex}(f) = \sqrt{\frac{2q(FG)I_{ex}}{1+\left(\frac{f}{f_0}\right)^2}} + I_{ROIC} \quad (1)$$

where $F$ is the excess noise factor, $I_{ROIC}$ is read-out noise current, and $f_0$ is the pixel's response frequency, which is related to the time constant $\tau$ by $f_0 = 1/(2\pi\tau)$. $\tau$ can be extracted from the response of the detector by measuring the time-response to a square pulse of light sent into the camera, as shown in Fig. 4(c) and Fig. 4(d). This test is performed at high frame rate, so that the photodetector will take multiple frames to equalize. The incoming light pulses are synchronized to the frame rate of the camera, illuminating the detector for exactly 128 frames and allowing it to settle for the following 128 frames. This synchronization allows multiple consecutive pulses to be averaged, producing clearer response curves and permitting fitting of the time constant at low optical powers, similar to the conditions under which the camera is intended to operate. As a result, the gain $G$ for 1 μm and 2 μm pixels are calculated to be ~22100 and ~5100, respectively. Comparing to similar technologies that produce a linear amplification of photocurrent (except low-dimensional technologies), the gain in this work is higher than most of the linear mode APDs[30,31], QD-FETs[32-34], and comparable to the best reported RTD[35]. Moreover, the response and speed at different powers are measured. The unity slope in the average response of the 1 μm and 2 μm pixels indicates good linearity (Fig. 5(a)). Besides, the speed is almost constant in the range of 100 fW to 1000 fW (Fig. 5(b)), which is promising for low light-level applications.

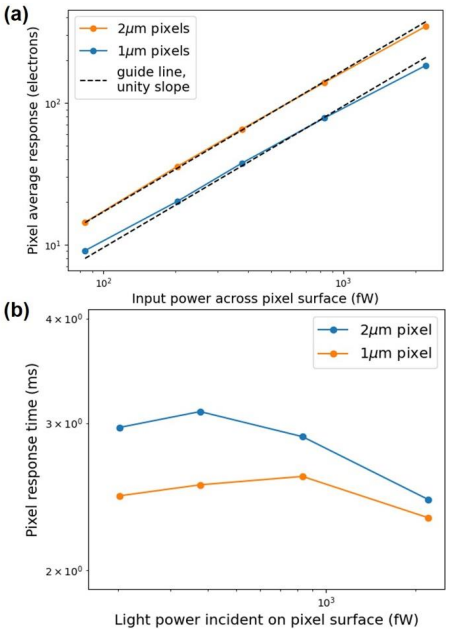


**Fig. 5** (a) Average response and (b) response time of the 1 μm and 2 μm pixels at different powers.

The sensitivity of the detector array can then be evaluated by its Noise Equivalent Photon (*NEPh*) level, which is the number of photons the detector would need to receive within its response time in order to produce a signal equal to the total noise of the system (i.e. *SNR*=1)[36]. The signal is the number of absorbed photons, which is an internal quantity (before the photodetector's amplification stage). An accurate assessment requires comparing it to the number of internal noise electrons. For a pixel with output (external) dark current $I_{ex}$ and a gain of $G$, the internal dark electrons per response time is $I_{ex} * 2.2\,\tau/(qG)$[37]. Time periods separated by the response time are uncorrelated by definition [29], so the dark noise obeys standard Poisson statistics (the integration time is longer than the pixel response time[29]) and produces $\sqrt{I_{ex} * 2.2\,\tau/(qG)}$ electrons of internal noise. The ROIC adds a read-out noise of $RON_{ROIC}$, but that is effectively suppressed by a factor of $G$ when compared to internal quantities and hence becomes negligible for our devices with a large internal gain. Therefore, the number of photons needed to equal this noise is given by Eq. (2), Accordingly, the calculated *NEPh* of the 1μm pixel in Fig. 4 is ~5.4 absorbed photons.

$$NEPh = \sqrt{\frac{I_{ex}*2.2\tau}{qG}} + \frac{RON_{ROIC}}{G} \approx \sqrt{2.2\frac{I_{ex}\tau}{qG}} \quad (2)$$

The illumination source we used is a fiber-coupled superluminescent diode (SLD), propagated through an expanding lens and several layers of diffusive media in order to create a uniformly glowing screen facing the camera. This setup provides equal illumination to every pixel, allowing fitting and analysis to be performed on every pixel simultaneously. It is thus possible to make histograms of calculated *NEPh* for statistically significant numbers of pixels, as shown in Fig. 6(a). On average, the detectors with 1 μm injectors exhibit *NEPh* of 19.9 photons at 200 K, which show better sensitivity than those with 2 μm injectors (33.5 photons, 200 K), respectively. In our previous work, we proposed a model for the *NEPh* of photodetectors[36]:

$$NEPh = \frac{1}{\eta} \cdot \frac{\gamma F}{2}\left(1 + \sqrt{1 + \frac{8}{\gamma F}\frac{C_T}{C_0}}\right) \quad (3)$$

in which $C_0=q^2/kT$, $q$ is the charge quanta, $k$ is the Boltzmann constant and $T$ is the temperature. $C_T$ is the capacitance of the base of the detector, $F$ is the excess noise factor that is predicted to be ~2 for phototransistors due to the charge number fluctuation at the base, $\gamma$ is the Fano factor (1 for Poisson processes) and $\eta$ is the quantum efficiency (considered as 1 since we are calculating the internal sensitivity based on the internal gain)[38-41]. Accordingly, by using the average *NEPh*, the $C_T$ of 1 μm and 2 μm detectors are 0.8 fF and 2.4 fF respectively, which shows good agreements with the parallel plate capacitor model with fringe field effect (0.72 fF and 2.44 fF)[42]:

$$C = \varepsilon_0\varepsilon_s\left(\frac{\pi r^2}{d} + rln\left(16\frac{\pi r}{d} - 1\right)\right) \quad (4)$$

where $\varepsilon_0$ is the vacuum permittivity, $\varepsilon_s$ is the dielectric constant of the semiconductor (~13 for InGaAs and InP), $r$ is the radius of the detector, and $d$ is the thickness of the depletion layer (~200 nm). Note that this is a first-order modeling, and we plan to perform further studies on the accurate equivalent capacitance model. Therefore, our measurement results show that photodetectors with smaller injectors, and thus smaller capacitance, are more sensitive. This result is consistent with the physical models. Moreover, we measured an almost identical distribution of *NEPh* at 200 K and 210 K as shown in Fig. 6(b) (average *NEPh*s at 200 K and 210 K are 19.9 and 19.1 photons, respectively), indicating a weak dependence of sensitivity to temperature. This weak temperature

dependency is in good agreement with our model (Eq. (3)). Note that, conversely, both the dark current and the response time of the devices change significantly with temperature (See Supplementary II). For the 1 μm detector, the average rise/fall time was ~2.5 msec at 200 K and ~0.95 msec at 210 K, resulting in maximum frame rates of about 180 FPS and 480 FPS respectively.

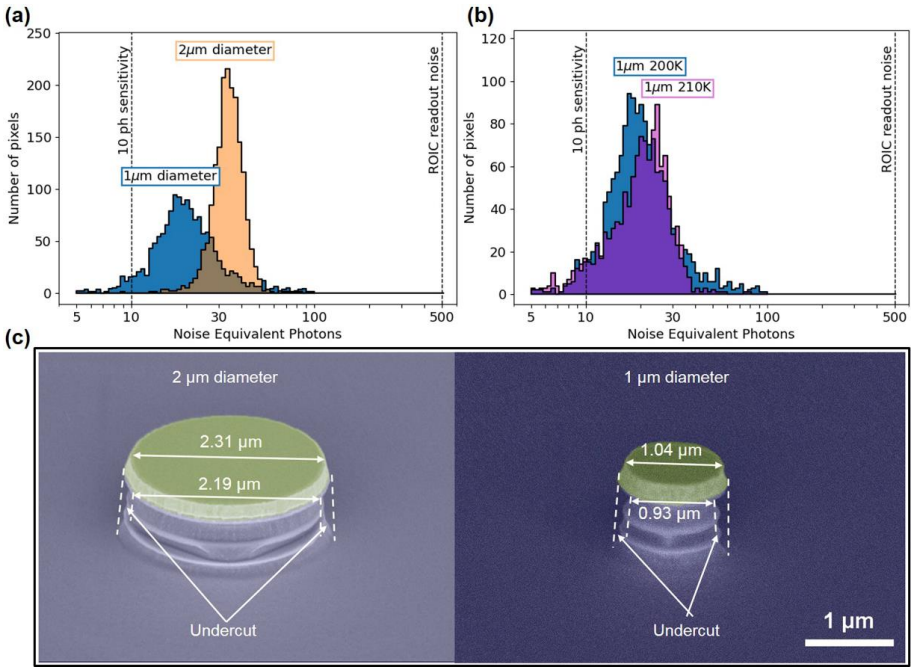


**Fig. 6** (a) Histograms of *NEPh* for the detector array in the 1 μm and 2 μm injector regions at 200 K. Displayed data comes from roughly 1900 pixels in 2μm region and 1650 pixels in 1μm region. (b) Histograms of *NEPh* for the 1 μm pixels at 200 K and 210 K. (c) SEM images of the 1 μm and 2 μm injectors showing the undercut.

The sensitivities of both detector populations are at least an order of magnitude lower than the readout noise of the ROIC, meaning that high internal gain makes the noise of the ROIC irrelevant. Besides, with comparable frame rate, most of the 1 μm pixels show better performance than the best reported commercial cameras in terms of sensitivity, speed and operating temperature (See Supplementary III). Among all the 1 μm pixels analyzed, more than 40 achieve sensitivity lower

than 10 photons. This high sensitivity indicates that the 1 μm HPT EI detector, which is capable of working with conventional ROIC chips, is a promising candidate for ultrasensitive imaging. According to the histogram in Fig. 6(a), the spread in sensitivity of 1 μm injectors is nearly twice that of the 2 μm injectors. This is likely due to small variations in the device processing. Fig. 6(c) demonstrates the details in the size of the injectors, in which the actual diameter of the 1 μm detector is ~900 nm after wet etching. The undercut formed after wet etching for the 1 μm and 2 μm injectors are almost the same (~110 nm) and thus the fluctuation in this undercut should also be the same. Therefore, the same fluctuation in radius means a larger percent change for a smaller injector and thus cause more variation in sensitivity. However, it is unlikely that size variation is the only reason for the observed variation in sensitivity, and further investigations are needed.

To conclude, we have presented an InGaAs/InP based phototransistor array integrated on a conventional CMOS ROIC chip. The array was made of a large number of devices with two different sizes in order to statistically evaluate the scaling effect on its sensitivity. This approach eliminates the run-to-run variation between different size devices, and also minimizes the effect of on-chip process variation on our final conclusion. Our detailed measurement reveals that the 1 μm and 2 μm detectors exhibit average noise-equivalent photon sensitivities of 19.9 and 33.5 photons, respectively. A good number of the 1 μm detectors show possibility of achieving below 10-photon level, despite the use of electronics with read noise of 500 electrons. With a comparable frame rate (~500 FPS), the sensitivity of the detector proposed in this work is better than the existing commercial cameras. Our experimental results confirm that lower capacitance pixels have higher sensitivities, and in a good quantitative agreement with the analytical model we proposed previously. Therefore, this work shows a promising detector for imaging thanks to its high sensitivity, and combined with the previous theoretical work on the scaling effect on sensitivity, provides a path toward realization of imaging arrays with higher sensitivity values. Our results also suggest that further attention is needed to achieve a high uniformity at such small size devices, and that bottom-up approaches might be indeed advantageous compared with our top-down method. We also intend to explore methods for boosting the pixel fill factors. For example, microlens arrays can focus incoming light in the sensitive region of each pixel surface, thus producing imaging sensors with simultaneously high fill factor and sensitivity.

**SUPPLEMENTARY MATERIAL**

See the supplementary material for the simulated band structures that show the function of the undoped InGaAsP layer, the dark current of the detectors at different temperatures, and the comparison of this work to state-of-art.

**ACKNOWLEDGEMENT**

This work was supported by W. M. Keck Foundation under a Research Grant in Science and Engineering and by partial funding from ARO Award No. W911NF-18-1-0429. This work was performed, in part, at the Center for Nanoscale Materials of Argonne National Laboratory. The use of the Center for Nanoscale Materials, an Office of Science user facility, was supported by the U.S. Department of Energy, Office of Science, Office of Basic Energy Sciences, under Contract No. DE-AC02-06CH11357. This work utilized the Northwestern University Micro/Nano Fabrication Facility (NUFAB), which is partially supported by the Soft and Hybrid Nanotechnology Experimental (SHyNE) Resource (NSF ECCS-1542205), the Materials Research Science and Engineering Center (NSF DMR-1720139), the State of Illinois, and Northwestern University. S.B. gratefully acknowledges support from the Ryan Fellowship and the International Institute for Nanotechnology at Northwestern University.

**DATA AVAILABILITY**

The data that support the findings of this study are available from the corresponding author upon reasonable request.

**REFENCE**

[1] B. Korzh, C. C. W. Lim, R. Houlman, N. Gisin, M. J. Li, D. Nolan, B. Sanguinetti, R. Thew, and H. Zbinden, Nat. Photonics, **9**, 163 (2015).

[2] J. Zhang, M. A. Itzler, H. Zbinden, and J. W. Pan, Light-Sci Appl, **4**, e286 (2015).

[3] R. H. Hadfield, Nat. Photonics, **3**, 696-705 (2009).

[4] O. Kahl, S. Ferrari, V. Kovalyuk, A. Vetter, G. Lewes-Malandrakis, C. Nebel, A. Komeev, G. Goltsman, and Pernice, Optica, **4**, 557 (2017).

[5] B. C. Du, C. K. Pang, D. Wu, Z. H. Li, H. Peng, Y. L. Tao, E. Wu, and G. Wu, Sci. Rep. **8**, 4198 (2018).

[6] E. J. Gansen, M. A. Rowe, M. B. Greene, D. Rosenberg, T. E. Harvey, M. Y. Su, R. H. Hadfield, S. W. Nam, and R. P. Mirin, Nat. Photonics, **1**, 585 (2007).

[7] J. C. Blakesley, P. See, A. J. Shields, B. E. Kardynal, P. Atkinson, I. Farrer, and D. A. Ritchie, Phys. Rev. Lett. **94**, 067401 (2005).

[8] M. H. Jiang, J. H. Liu, Y. Liu, G. Jin, J. Zhang, and J. W. Pan, Opt. Lett. **42**, 5090 (2017).

[9] Y. Liang, Q. Fei, Z. Liu, K. Huang, and H.Zeng, Photonics Res. **7**, A1 (2019).

[10] A. Pfenning, F. Hartmann, and S. Höfling, Proc. SPIE, 11386, 1138606 (2020).

[11] N. Jovanovic, F. Martinache, O. Guyon, C. Clergeon, G. Singh, T. Kudo, V. Garrel, K. Newman, D. Doughty, J. Lozi, J. Maies, Y. Minowa, Y. Hayano, N. Takato, J. Morino, J. Kuhn, E. Serabyn, B. Norris, P. Tuthill, G. Schworer, P. Stewart, L. Close, E. Huby, G. Perrin, S. Lacour, L. Gauchet, S. Vievard, N. Murakami, F. Oshiyama, N. Baba, T. Matsuo, J. Nishikawa, M. Tamura, O. Lai, F. Marchis, G. Duchene, T. Kotani, and J. Woillez, Publ. Astron. Soc. Pac. **127**, 890 (2015).

[12] R. J. McIntyre, IEEE Electron Device Lett. **ED-13**, 164 (1966).

[13] G. Konstantatos, M. Badioli, L. Gaudreau, J. Osmond, M. Bernechea, F. P. Garcia de Arquer, F. Gatti, and F. H. L. Koppens, Nat. Nanotechnol. **7**, 363 (2012).

[14] J. H. Jung, M. J. Yoon, J. W. Lim, Y. H. Lee, K. E. Lee, D. H. Kim, and J. H. Oh, Adv. Funct. Mater. **27**, 1604528 (2017).

[15] X. Liu, L. Gu, Q. Zhang, J. Wu, Y. Long, and Z. Fan, Nat. Commun. **5**, 4007 (2014).

[16] O. G. Memis, A. Katsnelson, S.-C. Kong, and H. Mohseni, Appl. Phys. Lett. **91**, 171112 (2007).

[17] O. G. Memis, J. Kohoutek, W. Wu, R. M. Gelfand and H. Mohseni, Opt. Lett. **35**, 2699 (2010).

[18] Y. Movassaghi, V. Fathipour, M. Fathipour, and H. Mohseni, J. Appl. Phys. **121**, 084501 (2017).

[19] M. Rezaei, M.-S. Park, C. L. Tan, and H. Mohseni, IEEE Electron Device Lett. **38**, 1051 (2017).

[20] O. G. Memis, J. Kohoutek, W. Wu, R. M. Gelfand and H. Mohseni, IEEE Photonics J. **2**, 858 (2010).

[21] V. Fathipour, T. Schmoll, A. Bonakdar, S. Wheaton and H. Mohseni, Sci. Rep., **7**, 1183 (2017).

[22] L. Y. Leu, J. T. Gardner, and S. R. Forrest, J. Appl. Phys. **69**, 1052 (1991).

[23] J. Yoon, S. Jo, I.-S. Chun, I. Jung, H.-S. Kim, M. Meitl, E. Menard, X. Li, J. J. Coleman, U. Paik, and J. A. Rogers, Nature, **465**, 329 (2010).

[24] U. Koren, T. R. Chen, C. Harder, A. Hasson, K. L. Yu, L. C. Chiu, S. Margalit and A. Yariv, Appl. Phys. Lett. **42**, 403 (1983).

[25] R. B. Jacobs-Gedrim, M. Shanmugam, N. Jain, C. A. Durcan, M. T. Murphy, T. M. Murray, R. J. Matyi, R. L. Moore, and B. Yu, ACS Nano, **8**, 514 (2014).

[26] P. Hu, Z. Wen, L. Wang, P. Tan, and K. Xiao, ACS Nano, **6**, 5988 (2012).

[27] S. Wolde, Y.-F. Lao, A. G. Unil Perera, Y. H. Zhang, T. M. Wang, J. O. Kim, T. Schuler-Sandy, Z.-B. Tian, and S. Krishna, J. Appl. Phys. **121**, 244501 (2017).

[28] C. Jelen, S. Slivken, T. David, M. Razeghi, and G. J. Brown, IEEE J. Quantum Electron. **34**, 1124 (1998).

[29] J. Rabinowitz, M. Rezaei, M.-S. Park, C. L. Tan, M. Ulmer, and H. Mohseni, Opt. Lett. **45**, 3009 (2020).

[30] G. Finger, I. Baker, D. Alvarez, D. Ives, L. Mehrgan, M. Meyer, J. Stegmeier, and H. J. Weller, Adaptive Optics Systems IV, **9148**, 914817 (2014).

[31] P. Feautrier, J.-L. Gach, and P. Wizinowich, Adaptive Optics for Extremely Large Telescopes 4–Conf. Proc. 1 (2015).

[32] G. Konstantatos and E. H. Sargent, Nat. Nanotech. **5**, 391 (2010).

[33] G. Konstantatos, I. Howard, A. Fischer, S. Hoogland, J. Clifford, E. Klem, L. Levina, and E. H. Sargent, Nature, **442**, 180 (2006).

[34] J.-S. Lee, M. V. Kovalenko, J. Huang, D. S. Chung, and D. V. Talapin, Nat. Nanotech. **6**, 348 (2011).

[35] A. Pfenning, F. Hartmann, F. Langer, S. Höfling, M. Kamp, and L. Worschech, Appl. Phys. Lett. **104**, 101109 (2014).

[36] M. Rezaei, M.-S. Park, C. Rabinowitz, C. L. Tan, S. Wheaton, M. Ulmer and H. Mohseni, Appl. Phys. Lett. **114**, 161101 (2019).

[37] S. Bianconi and H. Mohseni, Rep. Prog. Phys. **83**, 044101 (2020).

[38] Y. M. Blanter and M. Büttiker, Phys. Rep. **336**, 1 (2000).

[39] O. G. Memis, A. Katsnelson, S.-C. Kong, H. Mohseni, M. Yan, S. Zhang, T. Hossain, N. Jin, and I. Adesida, Opt. Express, **17**, 12701 (2008).

[40] Ó. García-Pérez, H. Sánchez-Martín, J. Mateos, S. Pérez, A. Westlund, J.Grahn, and T. González, J. Phys.: Conf. Ser. **647**, 012061 (2015).

[41] F. H. De La Moneda, E. R. Chenette, and A. Van Der Ziel, IEEE Trans. Electron Devices, **18**, 340 (1971).

[42] L. D. Landau and E. M. Lifschitz, "Electrodynamics of continuous media," Oxford, England, Permagon Press, 19 (1987).

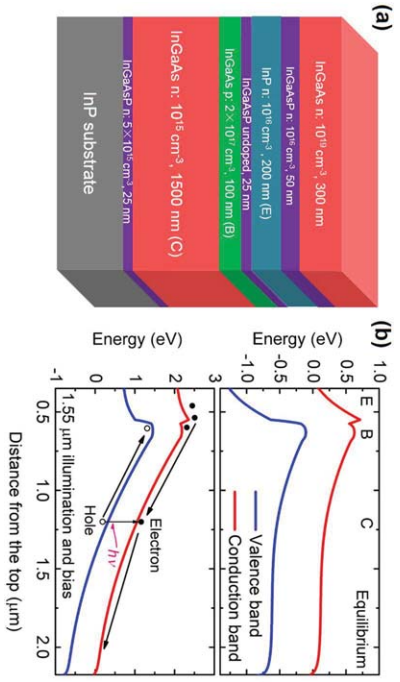

PLEASE CITE THIS ARTICLE AS DOI: 10.1063/5.0024259

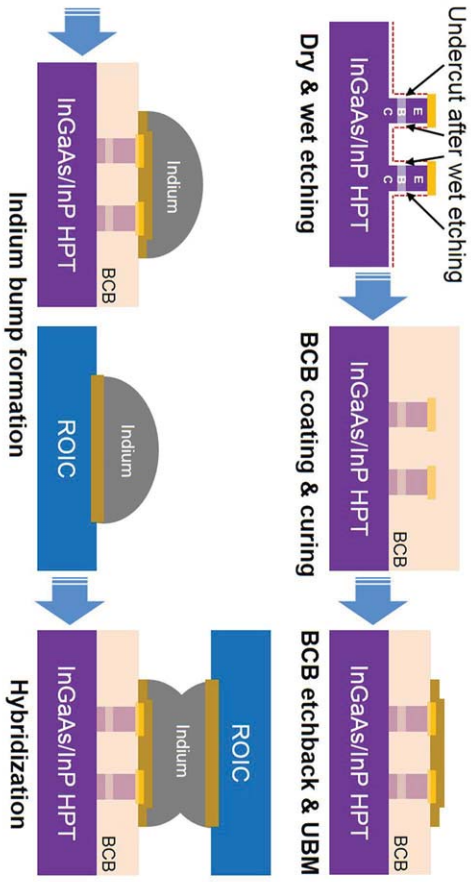

PLEASE CITE THIS ARTICLE AS DOI: 10.1063/5.0024259